Shock-induced melting of [100] lithium fluoride: Sound speed and Hugoniot measurements to 230 GPa

J. A. Hawreliak,[1] J. M. Winey,[1] Y. Toyoda,[1] M. Wallace,[1] and Y. M. Gupta[1,2]
[1]*Institute for Shock Physics, Washington State University, Pullman, Washington 99164-2816, USA*
[2]*Department of Physics and Astronomy, Washington State University, Pullman, Washington 99164-2814, USA*

(Received 12 September 2022; revised 15 November 2022; accepted 22 December 2022; published 13 January 2023)

Although [100] lithium flouride (LiF) is the most widely used optical window material in dynamic compression experiments, its high stress (>100 GPa) shock compression response, including melting, is not well understood. To address this need, we measured wave profiles in plate impact experiments to determine the Hugoniot states and longitudinal sound speeds in [100] LiF crystals shock compressed to 231 GPa. The measured peak states are fitted well by a linear shock velocity–particle velocity relation, providing an accurate determination of the LiF Hugoniot curve to significantly higher stresses than previous experiments. The longitudinal sound speeds show a near linear increase with density compression to 182 GPa. Between 182 GPa and 195 GPa, the sound speed and the longitudinal modulus decrease abruptly, due to shock-induced melting. The increasing sound speeds and moduli at higher stresses suggest that shock compressed LiF is fully liquid at 195 GPa and above, allowing determination of the Grüneisen parameter for liquid LiF. The melt stress determined here differs from that predicted by current multiphase equations of state for LiF. Our results provide important insight into the high stress solid and liquid states of shock compressed LiF and point to the need for an improved multiphase equation of state at high pressures and high temperatures.

DOI: 10.1103/PhysRevB.107.014104

I. INTRODUCTION

High purity lithium flouride (LiF) single crystals oriented along the [100] direction constitute the most commonly used optical windows in dynamic compression experiments. [100] LiF maintains transparency at 532 nm up to 210 GPa [1–3] in shock compression experiments and up to 900 GPa under shockless or ramp compression [4,5]. Due to its optical transparency, the high pressure response of LiF has been a subject of extensive research in theoretical [6–11] and experimental [2–5,12–24] studies.

Despite the strong interest in the high stress response of LiF, questions remain regarding its structural stability under shock compression above 100 GPa. Although the Hugoniot curves show no discontinuities to 150 GPa [14,18], a drop in the longitudinal sound speed for shocked LiF, attributed to melting, was reported at ∼140 GPa [18]. However, subsequent measurements [20] showed no drop in the longitudinal sound speed up to ∼170 GPa. Previous theoretical work [7,8] suggested that the reported loss of transparency above 210 GPa [1–3] was due to melting because of absorption differences between solid and liquid LiF.

For static compression experiments, LiF's optical transparency, low thermal conductivity, chemical inertness, and low x-ray absorption and scattering make it a potential pressure-transmitting medium and a pressure standard [21–23]. Using laser heating in diamond anvil cell experiments, the melt curve for LiF has been reported to 100 GPa [24]. Combining these results with quantum molecular dynamics calculations, melting on the Hugoniot was predicted to occur at ∼140 GPa [11]. A theoretical study [9] has even suggested a solid-solid phase transformation at ∼140 GPa.

In addition to the conflicting results regarding the LiF structural response above 100 GPa, we note that the most widely used LiF Hugoniot [2] is based on experimental data to ∼100 GPa. Since LiF is used as a window material to stresses > 200 GPa, shock compression data at higher stresses are desirable.

Using wave profile measurements in well characterized plate impact experiments, we present Hugoniot states and sound speed results in [100] LiF shock compressed to 231 GPa. The experimental results presented here are intended to address the issues summarized above regarding the high stress LiF response.

The paper is organized as follows. Experimental methods and results are presented in Secs. II and III, respectively. Analysis of the results and determination of the Hugoniot curve, sound speeds, and Grüneisen paramenter in the liquid state are given in Sec. IV. Equation of state implications are also discussed in Sec. IV. The main findings from the present work are summarized in Sec. V.

II. EXPERIMENTAL METHODS

[100] LiF single crystals in the present work were cut from UV grade ultrapure rods and polished to an optical finish by Asphera Incorporated. The crystals were within 1^o of the specified orientation, as verified by Laue x-ray diffraction. The average measured density and longitudinal sound speed

TABLE I. Experimental Parameters

Experiment No.	Configuration[a]	Flyer Velocity (km/s)	Sample thickness (mm)	Shock transit time (ns)	Rarefaction transit time (ns)
1 (22-2sh16)[b]	DI	6.905 ± 0.006	1.543 ± 0.002	124.0 ± 0.8	62.7 ± 1.0
2 (21-2sh25)[c]	DI	6.920 ± 0.016	1.435 ± 0.002	114.0 ± 0.3	59.1 ± 0.5
3 (21-2sh17)[c]	DI	7.237 ± 0.002	1.517 ± 0.002	117.0 ± 0.3	71.3 ± 0.5
4 (21-2sh21)[c]	DI	7.275 ± 0.012	1.524 ± 0.002	118.0 ± 0.6	72.3 ± 0.5
5 (21-2sh46)[c]	DI	7.543 ± 0.010	1.512 ± 0.002	115.0 ± 0.3	69.8 ± 0.5
6 (21-2sh43)[c]	DI	7.543 ± 0.005	1.530 ± 0.002	116.0 ± 0.3	72.7 ± 0.5
7 (21-2sh22)[cd]	DI	7.683 ± 0.006	1.470 ± 0.002	110.0 ± 0.3	–
8 (22-2sh14)[b]	CuB	7.299 ± 0.009	1.406 ± 0.002	102.0 ± 0.2	64.8 ± 1.0
9 (22-2sh15)[b]	CuB	7.304 ± 0.017	1.327 ± 0.002	96.3 ± 0.2	61.2 ± 1.0

[a]Direct Impact (DI) or use of copper buffer (CuB).
[b]Measurements made with PDV.
[c]Measurements made with VISAR.
[d]Signal lost from Sample/Window interface after shock arrival.

(2.64 g/cm^3 and 6.60 km/s, respectively) were in good agreement with the published values [2,25–27].

Plate impact experiments were conducted using the two-stage gas gun facility at the Institute for Shock Physics at Washington State University and the experimental parameters for all nine experiments are listed in Table I. The experimental configuration, shown in Fig. 1, was similar to that reported recently [20]. The target assembly consisted of two stacked [100] LiF disks, with the first disk acting as the sample and the second disk acting as the window. Prior to bonding, aluminum mirrors were vapor-deposited onto the impact side of the LiF sample and onto the central region of the sample/window interface; for experiments 5, 6, 8, and 9, gold mirrors were used. For most of the experiments, the LiF target assembly was impacted directly by a platinum flyer [Fig. 1(a)]. For experiments 8 and 9, the platinum flyer impacted a copper buffer which was bonded to the LiF target assembly [Fig. 1(b)].

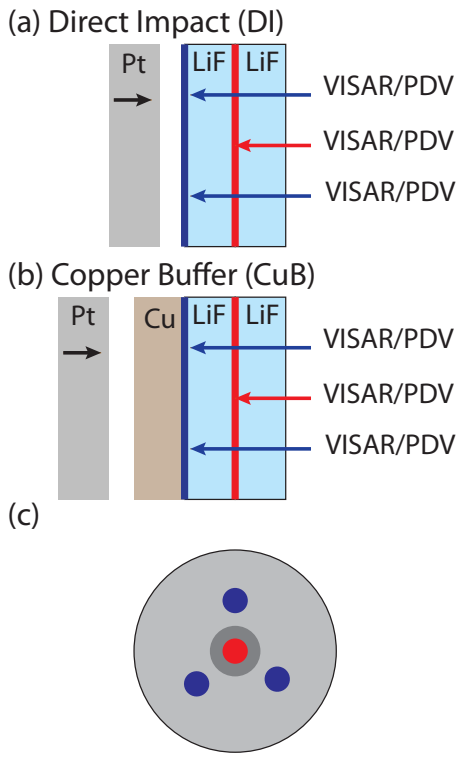

FIG. 1. Experimental configuration utilizing (a) direct impact (DI) and (b) a copper buffer (CuB). All experiments used a platinum impactor. (c) Rear view of the target showing the VISAR/PDV probe arrangement. The blue circles denote probes at the LiF front surface and the red circle indicates the probe at the LiF sample/window interface.

Particle velocity histories were measured at the impactor/sample interface (or buffer/sample interface) and at the sample/window interface using laser interferometry (velocity interferometer system for any reflector (VISAR) [28] and/or photon doppler velocimetry (PDV) [29]). The three probes at the impactor/sample interface [Fig. 1(b)] were positioned at 120^o intervals to determine the impact tilt and to provide an accurate fiducial for shock wave entry into the sample. The probe at the sample/window interface used a dual velocity-per-fringe (VPF) configuration to ensure an unambiguous particle velocity measurement.

Due to the transparency of the LiF sample and window, the experimental configuration used in this work (Fig. 1) provided an absolute determination of both the shock velocity and the release wave speed, discussed further in Section IV.

III. EXPERIMENTAL RESULTS

The measured wave profiles were corrected for shock-induced changes in the LiF refractive index [2] and the corrected profiles are shown in Fig. 2. The wave profiles measured at the front surface of the LiF samples are shown in Fig. 2(a). Of the three profiles measured for each experiment, only one is shown; the other two are similar. As shown in the figure, the measured particle velocity was maintained until the arrival of the release wave originating at the back of the platinum impactor. Figure 2(b) shows the wave profiles measured at the LiF sample/window interface; all profiles show a single sharp jump to the peak state, which is maintained until the arrival of the release wave.

In experiments 3 - 9, a very small decay in the particle velocity was observed after the arrival of the shock wave.

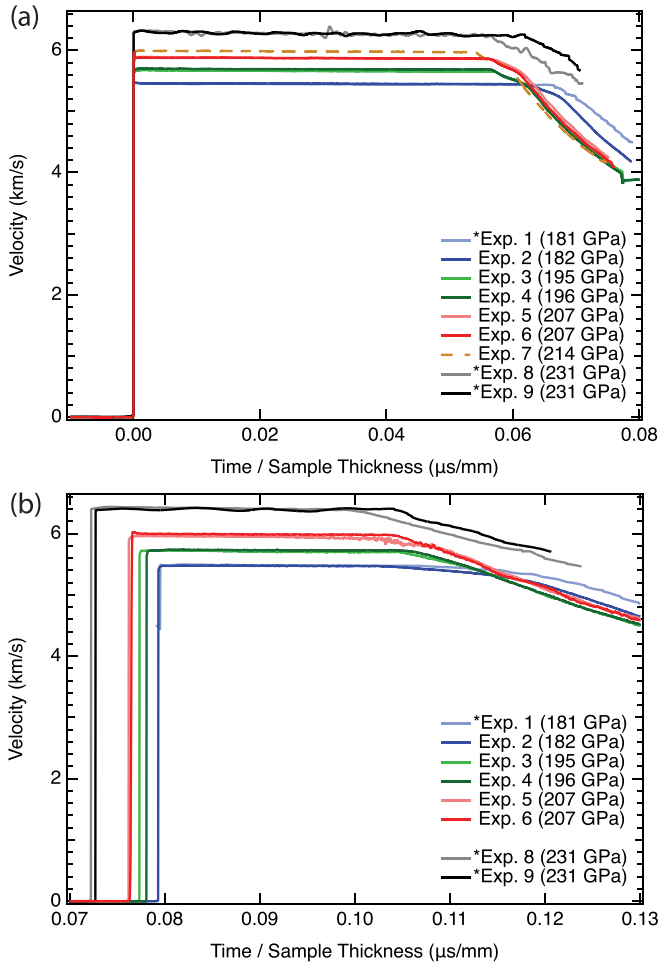

FIG. 2. Wave profiles measured at the (a) LiF front surface and (b) LiF sample-window interface. The profiles are color coded and labeled by experiment. The asterisk denotes profiles measured using PDV, while the remaining profiles were measured using VISAR. The velocity profile for experiment 7 is dashed since only the wave profile at the LiF front surface was measured in this experiment.

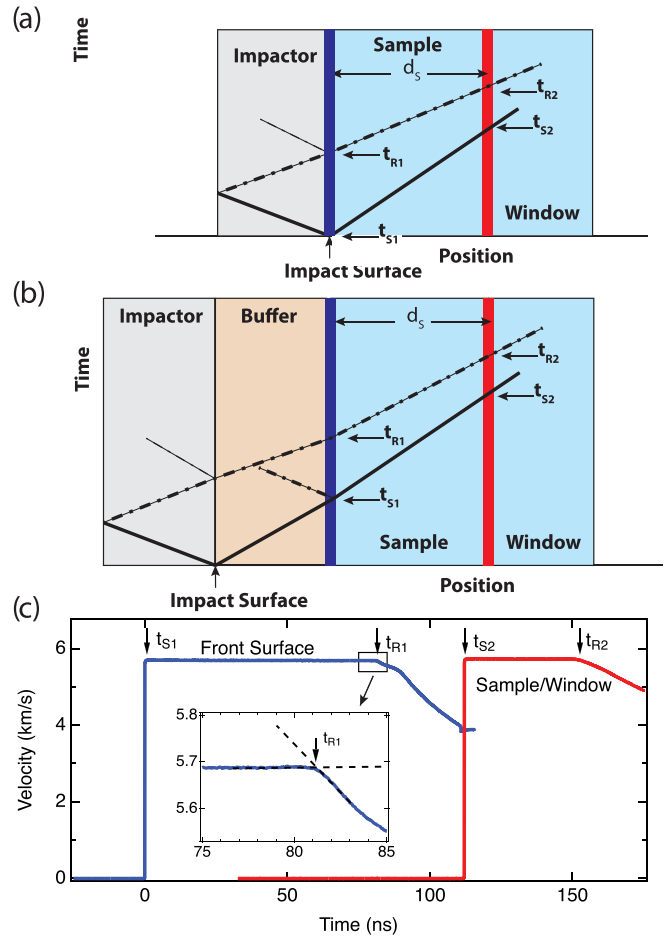

FIG. 3. Lagrangian distance-time diagrams for wave propagation in (a) direct impact and (b) copper buffer configurations. Solid and dot-dashed lines denote the shock and rarefaction waves, respectively. (c) Representative results from experiment 4 for the probes at the LiF front surface (blue) and the LiF sample/window interface (red), with identifying markers to signify t_{S1}, t_{S2}, t_{R1}, and t_{R2}. The inset shows the approach for determining the release wave arrival times.

Furthermore, the peak particle velocity at the LiF sample/window interface was very slightly larger than the particle velocity measured at the front of the LiF sample. Although these effects were reproducible, their magnitudes are within the experimental uncertainties. Hence, they are not discussed in the remainder of the paper.

IV. ANALYSIS AND DISCUSSION

To facilitate the data analysis, Figs. 3(a) and 3(b) show Lagrangian position-time diagrams for wave propagation through the platinum impactor, buffer, sample, and window for both target configurations (see Fig. 1). The shock and rarefaction waves are denoted by solid and dot-dashed lines respectively. For the buffer configuration, the thickness of the impactor and buffer are such that the rarefaction wave from the back surface of the platinum reaches the platinum-copper interface before the rarefaction wave originating at the Cu/LiF interface.

For both configurations, the experimental observables are the same: shock arrival time at the front of the LiF sample (t_{S1}), shock arrival time at the sample/window interface (t_{S2}), rarefaction arrival time at the front of the LiF sample (t_{R1}), and rarefaction arrival time at the sample/window interface (t_{R2}).

The measured arrival times for a representative experiment (experiment 4) are shown in Fig. 3(c). The arrival times at the LiF front surface are the averages for all three front surface probes. Figure 3(c) inset shows how the rarefaction wave arrival time t_{R1} was determined (intersection of linear fits to the peak velocity and the initial release). The same technique was used to determine t_{R2} at the sample/window interface. The wave transit times, listed in Table I, provided a direct determination of the shock speed (U_S) and the Lagrangian longitudinal sound speed (c_L) in the LiF using

$$U_S = \frac{d_S}{t_{S2} - t_{S1}}, \tag{1}$$

TABLE II. Hugoniot Results.

Experiment No.	Shock Velocity U_S (km/s)	Particle Velocity u_P (km/s)	Stress P_x (GPa)	Density ρ (g/cm^3)	Volume Compression V/V_0
1	12.57 ± 0.05	5.462 ± 0.011	181.3 ± 0.7	4.67 ± 0.02	0.565 ± 0.002
2	12.59 ± 0.05	5.474 ± 0.017	181.9 ± 0.8	4.67 ± 0.02	0.565 ± 0.002
3	12.93 ± 0.05	5.715 ± 0.011	195.1 ± 0.7	4.73 ± 0.02	0.558 ± 0.002
4	12.92 ± 0.08	5.749 ± 0.016	196.0 ± 1.2	4.76 ± 0.03	0.555 ± 0.004
5	13.18 ± 0.05	5.955 ± 0.014	207.2 ± 0.8	4.82 ± 0.02	0.548 ± 0.002
6	13.18 ± 0.05	5.955 ± 0.012	207.2 ± 0.8	4.82 ± 0.02	0.548 ± 0.002
7	13.37 ± 0.05	6.058 ± 0.012	213.9 ± 0.9	4.83 ± 0.02	0.547 ± 0.002
8	13.82 ± 0.03	6.328 ± 0.054	230.9 ± 2.0	4.87 ± 0.05	0.542 ± 0.006
9	13.82 ± 0.03	6.333 ± 0.054	231.1 ± 2.0	4.88 ± 0.05	0.542 ± 0.006
W1[a]	10.77 ± 0.04	4.153 ± 0.009	118.1 ± 0.4	4.30 ± 0.01	0.614 ± 0.002
W2[a]	11.45 ± 0.04	4.642 ± 0.010	140.3 ± 0.5	4.44 ± 0.02	0.594 ± 0.002
W3[a]	11.85 ± 0.05	4.966 ± 0.012	155.4 ± 0.6	4.54 ± 0.02	0.581 ± 0.002
W4[a]	12.24 ± 0.05	5.241 ± 0.011	169.0 ± 0.6	4.62 ± 0.02	0.571 ± 0.002

[a]Redetermined from Ref. [20] using impedance matching.

$$c_L = \frac{d_S}{t_{R2} - t_{R1}}, \tag{2}$$

where d_S is the sample thickness.

A. Determination of Hugoniot states

Using the measured shock velocities and flyer velocities, the Hugoniot states for each experiment were determined using impedance matching [30] and are listed in Table II. Table II also includes the Hugoniot states from Wallace *et al.* [20] that were redetermined using impedance matching, to ensure consistency between Ref. [20] and the present results. The uncertainties in Table II were calculated using a Monte Carlo method with 10^5 points.

Figure 4(a) shows the shock velocity–particle velocity plot for the results from Table II, including the reanalyzed results from Ref. [20]. For most of the data in Fig. 4(a), the uncertainties are smaller than the symbols used on the plot. All the U_S−u_P states from Table II are fitted well using a straight line

$$U_S = (5.144 \pm 0.010)\text{km/s} + (1.355 \pm 0.004)u_P, \tag{3}$$

arising from a global fit to the current results and previously published data, as discussed in Appendix A. Details regarding the impedance matching calculations are summarized in Appendix B.

Figure 4(b) shows the stress–volume compression results corresponding to the results and the linear fit [Eq. (3)] in Fig. 4(a); the grey region indicates the uncertainty in the fit. The results in Fig. 4 provide an accurate determination of the LiF Hugoniot curve to 230 GPa, significantly extending the experimental range of previous Hugoniot determinations [2,14,18]. We note that the LiF shock response is described well by a single smooth Hugoniot curve with no discontinuities.

B. Sound speeds and longitudinal Moduli

From the Lagrangian sound speeds obtain using Eq. (2), the Eulerian sound speeds (which account for the compression of the shocked sample) c_E can be determined using

$$c_E = \frac{\rho_0}{\rho} c_L, \tag{4}$$

where ρ is the density in the shocked state (Table II) and ρ_0 is the ambient density. The sound speeds from the present work and from Ref. [20] are listed in Table III. The Eulerian

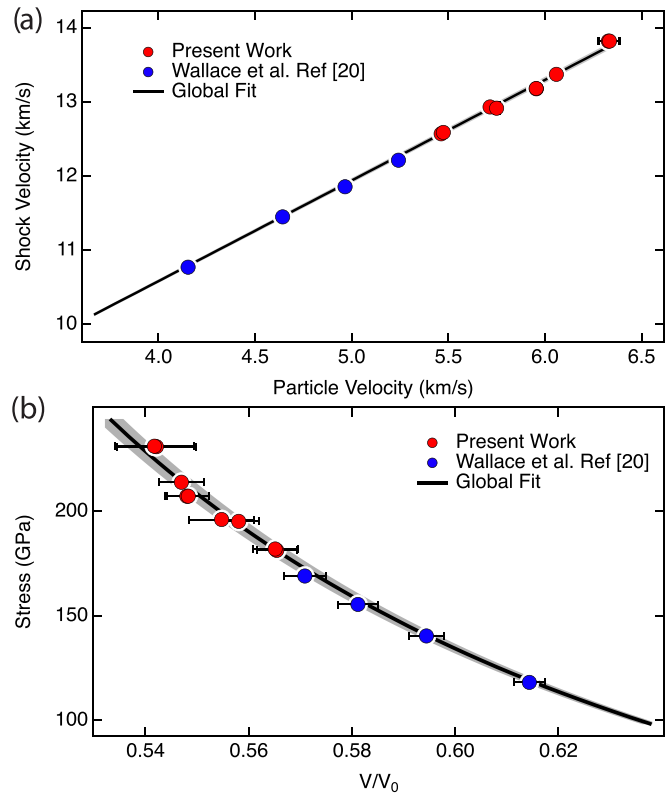

FIG. 4. Hugoniot states from the present work and the reanalyzed results from Wallace *et al.* [20]. (a) Shock velocity - particle velocity results and the global fit from Eq. (3). (b) Stress - volume compression results corresponding to (a). The grey region indicates the uncertainty in the fit.

TABLE III. Sound speeds, longitudinal moduli, and the calculated Grüneisen parameter.

Experiment No.	Lagrangian Sound Speed c_L (km/s)	Eulerian Sound Speed c_E (km/s)	Longitudinal Modulus L (GPa)	Grüneisen Parameter Γ	Γ/V (g/cm^3)
1	24.6 ± 0.6	13.9 ± 0.4	902 ± 55	–	–
2	24.3 ± 0.2	13.7 ± 0.2	878 ± 29	–	–
3	21.3 ± 0.2	11.9 ± 0.1	666 ± 19	1.10 ± 0.04	5.2 ± 0.2
4	21.1 ± 0.2	11.7 ± 0.2	650 ± 23	1.19 ± 0.06	5.6 ± 0.3
5	21.7 ± 0.2	11.9 ± 0.2	679 ± 20	1.11 ± 0.04	5.3 ± 0.2
6	21.0 ± 0.2	11.5 ± 0.1	641 ± 18	1.23 ± 0.04	5.9 ± 0.2
7	–	–	–	–	–
8	22.4 ± 0.6	12.1 ± 0.5	718 ± 60	1.21 ± 0.10	5.9 ± 0.5
9	22.4 ± 0.6	12.2 ± 0.5	726 ± 60	1.20 ± 0.10	5.8 ± 0.5
W1	20.6 ± 0.2[a]	12.7 ± 0.1[b]	684 ± 17	–	–
W2	22.4 ± 0.2[a]	13.3 ± 0.2[b]	785 ± 22	–	–
W3	23.7 ± 0.2[a]	13.8 ± 0.2[b]	864 ± 26	–	–
W4	24.1 ± 0.2[a]	13.8 ± 0.2[b]	880 ± 28	–	–

[a]From Ref. [20].
[b]Redetermined from Ref. [20] using Hugoniot density from Table II.

sound speeds from Table III, along with those from Ref. [18], are plotted as a function of stress in Fig. 5(a), and density compression ($\mu = \rho/\rho_0 - 1$) in Fig. 5(b). As discussed in Ref. [20], the low sound speed datum at 150 GPa reported in Ref. [18] is likely an experimental error and is not considered further in the remainder of the present work. Although variations in the rate of sound speed increase with compression cannot be ruled out, Fig. 5(b) shows that the longitudinal sound speeds from Table III and from Ref. [18] are fitted well by a straight line up to 182 GPa ($\mu = 0.77$):

$$c_E^{\text{solid}}[\text{km/s}] = (6.57 \pm 0.04) + (9.69 \pm 0.11)\mu. \quad (5)$$

Equation (5) was obtained by using a linear weighted fit [31] that included the ambient longitudinal sound speed for [100] LiF [25]. Between 182 GPa and 195 GPa ($\mu \approx 0.775$), there is a significant drop in the sound speed before increasing again at higher stresses.

The isentropic longitudinal elastic moduli in the shocked state were determined from the Eulerian sound speeds using

$$L = \rho c_E^2. \quad (6)$$

The results shown in Fig. 5(c) and in Table III demonstrate the strong increase in the longitudinal incompressibility (8-fold at 182 GPa) for solid LiF under uniaxial strain, despite the temperature increase due to shock compression. Similar to the Eulerian sound speed, the longitudinal modulus drops significantly between 182 GPa and 195 GPa. Despite some scatter in the results at 207 GPa, there is an overall increasing trend for the moduli at 195 GPa and above.

The rapid decrease in the longitudinal sound speed (and the associated modulus) between 182 and 195 GPa is a well-established [32–35] signature of the melting transition in shock compression experiments. Above 195 GPa, the increasing trend in sound speeds and moduli makes a good case that LiF is fully liquid at 195 GPa. Furthermore, the liquid phase response at and above 195 GPa is fully consistent with the thermodynamic requirement for the propagation of a stable shock in a liquid [36,37]: the slope of the Hugoniot curve must be steeper than the slope of the isentrope, which in turn must be steeper than the Rayleigh line. This requirement is expressed as

$$\left(-\frac{\partial P}{\partial V}\right)_{\text{RH}} > \left(-\frac{\partial P}{\partial V}\right)_{\text{S}} > \frac{P_H - P_0}{V_0 - V}, \quad (7)$$

where P_H and V are the pressure and volume on the Hugoniot, and the derivatives are obtained in the shock compressed state. The measured LiF response at 182 GPa and below does not meet this requirement, indicating that shocked LiF is not liquid at these stresses.

We note that the stress threshold for melting determined here is lower than that suggested previously (> 210 GPa) based on the loss of optical transparency for shocked LiF [1–3,7,8]. In view of the present results, the suggested link [7,8] between loss of transparency and melting needs to be reevaluated.

C. Grüneisen parameter

The results shown in Tables II and III are sufficient to determine the Grüneisen parameter (Γ) for shock compressed liquid LiF (195 GPa and above) using the following relation [38,39]:

$$\frac{\Gamma}{V} = \left(\frac{2}{V_0 - V}\right) \frac{\left(\frac{\partial P}{\partial V}\right)_{\text{RH}} - \left(\frac{\partial P}{\partial V}\right)_{\text{S}}}{\left(\frac{\partial P}{\partial V}\right)_{\text{RH}} - \left(\frac{P_H - P_0}{V_0 - V}\right)}. \quad (8)$$

The slopes of the Hugoniot curve and the isentrope were determined using Eq. (3) and the sound speeds from Table III, respectively. We note that the above approach for determining Γ/V is valid only for the liquid phase.

Table III lists both Γ and Γ/V for liquid LiF, and Γ/V values are plotted in Fig. 6. Due to the scatter in the results and the limited density range, we cannot infer the precise functional form for $\Gamma(V)$. Both constant Γ/V [Fig. 6(a)] and constant Γ [Fig. 6(b)] provide a reasonable match to the data. However, we note that the Γ/V values for liquid LiF, shown in Fig. 6(a), are significantly larger than the ambient value for solid LiF ($\Gamma/V = 4.30$ g/cm^3 [14]).

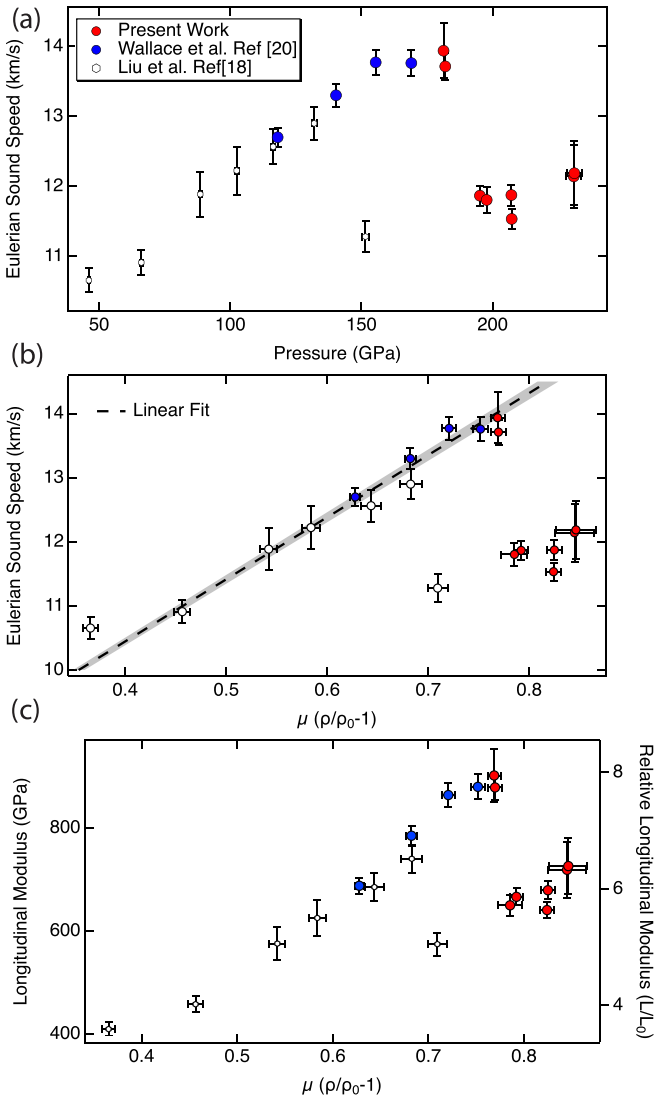

FIG. 5. (a) Eulerian sound speeds versus pressure, (b) Eulerian sound speeds versus density compression, (c) longitudinal elastic moduli versus density compression. In all three plots, the red circles are the current results, the blue circles are from Ref. [20], and the black open circles are from Ref. [18]. The black dashed line in (b) is a linear fit [31] to the sound speeds in the solid phase, including the ambient value [25]. The gray band shows the 1σ uncertainty bounds for the fit.

D. EOS comparisons

Despite the lack of temperature measurements in shock compressed LiF, useful insights can be gained by comparing T-P predictions of current equation of state (EOS) models with our experimental results. Since three of the EOS models (Myint *et al.* [11], LEOS 2240, and SESAME 7271v3; the latter two models were presented in Ref. [11]) provide a similar T-P curve for the solid phase LiF Hugoniot, we have focused on these three EOS models.

The T-P plot in Fig. 7 provides the following: solid-liquid phase boundaries from the three EOS models; static pressure measurements and MD simulations from Ref. [24]; the solid phase Hugoniot curve (consistent with all three EOS models);

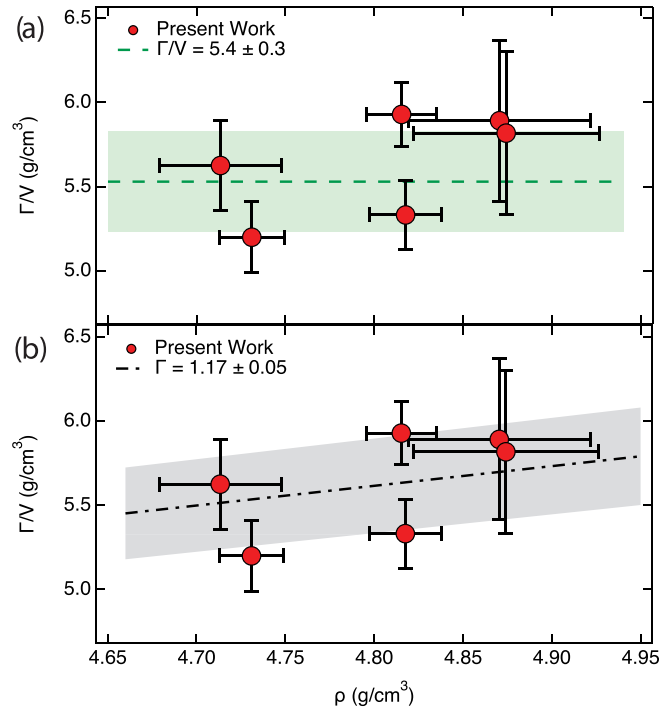

FIG. 6. The calculated Grüneisen parameter Γ, plotted as Γ/V versus ρ, for LiF in the liquid phase. (a) The green dashed line is the fit assuming Γ/V is constant. (b) The black dot-dashed line is the fit assuming Γ is constant. In both cases, the uncertainty in the fit is expressed by the shaded region.

and the stress range for melting (onset to completion) in the present work. The melt curve calculated by Myint *et al.* predicts a very low stress (∼140 GPa) for the onset of shock melting. The LEOS 2240 and MD simulations also underpredict the stress for shock melting, but predict a higher melting

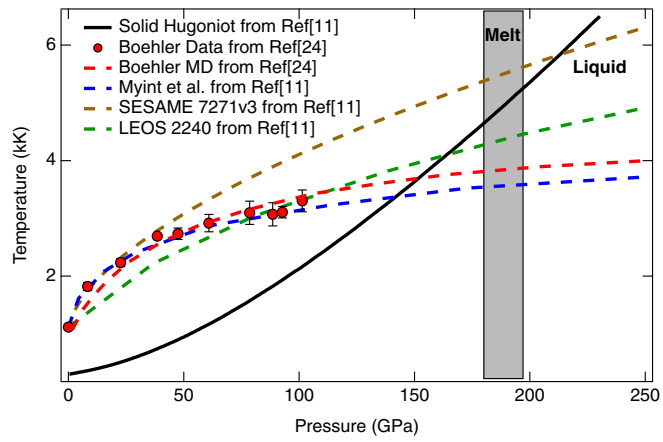

FIG. 7. Temperature versus pressure for LiF. The black solid curve is the Hugoniot curve for solid LiF that is consistent with the Myint *et al.* EOS [11], Sesame 7271v3, and LEOS 2240. The gray shaded region indicates the stress range over which melting was observed in Fig. 5(a). The dashed curves are the melt curves determined by the different EOS models [11] or calculated using MD simulations [24].

stress than the Myint *et al.* EOS. The SESAME 7271v3 overpredicts the melting stress.

In addition to the melting stress threshold, sound speed measurements in the solid and liquid phases and the liquid state Grüneisen parameter provide important constraints for future improvements in multiphase EOS models for LiF.

Although Smirnov [9] has developed a multiphase LiF EOS, we chose not to include that in Fig. 7 for the following reasons. Unlike the three EOS models shown in Fig. 7, the EOS model in Ref. [9] predicted a B1-B2 structural phase transformation at ∼140 GPa in shock compressed LiF. Furthermore, the predicted B1-B2 transformation was accompanied by a considerable drop in the calculated longitudinal sound speed and a significant volume collapse. Because our experimental results contradict these calculated predictions, the solid phase EOS in Ref. [9] will need to be revised.

V. SUMMARY AND CONCLUSION

The high stress (>100 GPa) response of [100] LiF single crystals, the most widely used optical window material in dynamic compression experiments, was determined using wave profile measurements in high velocity, plate impact experiments. Hugoniot states and sound speeds were determined to 231 GPa. The main findings from our work follow:

(1) Combining our results with previously published results (at lower stresses), an accurate LiF Hugoniot was established to 231 GPa. A linear U_S-u_p fit provides an excellent representation for the Hugoniot curve.

(2) Longitudinal sound speeds in shock compressed states show a continuous increase to 182 GPa (∼44% volume compression), resulting in an 8-fold increase in the longitudinal modulus (at 182 GPa) compared to the ambient value.

(3) Between 182 GPa and 195 GPa, the longitudinal sound speed drops significantly, providing a good signature of the shock-induced melting transition. Increasing sound speeds at higher stresses provide evidence that melting is completed at 195 GPa. Sound speeds at and above 195 GPa also meet the thermodynamic requirements for a stable shock in a fluid.

(4) The melting stress determined here differs from predictions of multiphase equations of state (Myint *et al.* [11], LEOS 2240, and SESAME 7271v3) and from previously suggested values based on the loss of optical transparency in shock compressed LiF [1,2,7,8].

(5) The Grüneisen parameter for liquid LiF was determined to 231 GPa and Γ/V for liquid LiF differs significantly from the solid value at ambient conditions.

The LiF Hugoniot determined in this work has extended previous experimental results to significantly higher stresses and provided the first accurate determination of the LiF Hugoniot through the melt transition and in the liquid phase. We note that the upper bound for optical transmission in shock compressed LiF was not established in our work and [100] LiF may continue to function well as an optical window in the liquid phase at pressures higher than those achieved in this work.

Similar to previous shock wave experiments on silver [40] and soda lime glass [39], the Hugoniot curve for LiF shows no features indicative of the melt transition, suggesting little change in volume between the solid and liquid phases. These findings emphasize the importance of sound speed measurements for understanding the high stress shock response of solids.

Experimental determination of the Hugoniot curve, sound speeds, shock melting stress, and liquid phase Grüneisen parameter presented here point to the need for improved multiphase equations of state for LiF at high pressures and temperatures, and provide useful constraints for EOS developments. Due to the extensive use of [100] LiF as an optical window in dynamic compression experiments, an accurate multiphase LiF EOS would constitute an important contribution to the field.

ACKNOWLEDGMENTS

The authors gratefully acknowledge N. Arganbright and K. Zimmerman for their expert assistance with the experiments. This work was supported by the U.S. Department of Energy (DOE) National Nuclear Security Administration (NNSA) under Cooperative Agreement No. DE-NA0003957.

APPENDIX A: GLOBAL HUGONIOT FIT FOR LiF

Figure 8(a) shows a plot of U_S-u_P results from Table II, along with the results reported previously [3,12–20]. The results from Carter *et al.* [14] were reanalyzed using the 2024 Aluminum Hugoniot [27].

The experimental results in Fig. 8(a) were fitted using a weighted orthogonal distance regression method [41,42] and the best linear fit is given by Eq. (3). We did not include the data from Refs. [12] and [13] as the uncertainties in the results are unknown, and the Ref. [13] results are significant outliers from the other results. Because it is difficult to visually resolve the uncertainties in Fig. 8(a), Figs. 8(b) and (c) show the shock speed and particle speed residuals, respectively, for all the data. The grey region in Figs. 8(b) and 8(c) represents the uncertainty in the linear fit [Eq. (3)]. In Figs. 8(a) and 8(b) we have also plotted the published linear fit from Rigg *et al.* [2]. We emphasize that all the data are fitted well by a single linear U_S-u_P relation over the entire range of shock speeds; and the uncertainties in the fit parameters [Eq. (3)] are significantly smaller than those reported previously for the LiF Hugoniot [2,18].

Figure 9 shows the $P_x - V/V_0$ Hugoniot for the results shown in Fig. 8(a). The dashed curve is the $P_x - V/V_0$ curve corresponding to the linear $U_s - u_p$ fit [Eq. (3)]; the grey region corresponds to the uncertainty in the fit. To summarize, Figs. 8 and 9 provide an accurate determination of the LiF Hugoniot curve to over 230 GPa.

APPENDIX B: IMPEDANCE MATCHING

The impedance matching calculations used for our two experimental configurations are summarized below. The buffer configuration [Fig. 1(b)] required a determination of the copper release isentrope.

1. Direct impact

Figure 10(a) shows a graphical representation of the impedance matching [30] for experiment 2. The pressure and

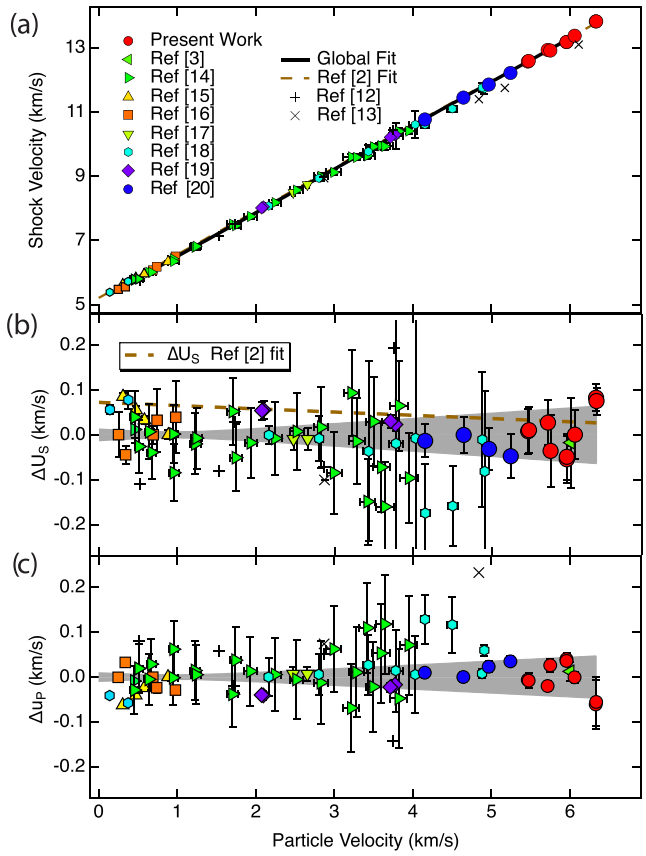

FIG. 8. U_S-u_P Hugoniot data for LiF from current study and from Refs. [3,12–20]. (a) U_S versus u_P for all available data, together with the linear fit from Eq. (3). (b) and (c) show the residuals of the fits in both shock velocity and particle velocity, respectively; the uncertainty in the fit is shown in grey. The symbol legend in (a) applies also to (b) and (c).

particle velocity upon impact are obtained from the following equations.

$$P_{\mathrm{LiF}}(u_P) = \rho_{0_{\mathrm{LiF}}} U_{S_{\mathrm{LiF}}}\ u_P \tag{B1}$$

$$P_{\mathrm{Pt}}(u_P) = \rho_{0_{\mathrm{Pt}}}(C_{0_{\mathrm{Pt}}} + S_{\mathrm{Pt}}(u_F - u_P))(u_F - u_P), \tag{B2}$$

where $\rho_{0_{\mathrm{LiF}}}$ is the initial density of the LiF sample, $U_{S_{\mathrm{LiF}}}$ is the measured shock velocity, u_F is the flyer velocity, u_P is the particle velocity, and the coefficients for the platinum Hugoniot curve are given in Table IV [43]. The inset in Fig. 10(a) shows the associated uncertainties calculated using a Monte Carlo method of uncertainty propagation.

2. Buffer configuration

In the buffer configuration, the copper buffer introduces additional wave interactions which need to be considered in the impedance matching analysis. Due to the shock impedance differences between the platinum, copper, and LiF, a peak stress of 231 GPa was attained in the LiF. In contrast, direct impact of the platinum onto LiF would provide less than 200 GPa at the same impact velocity.

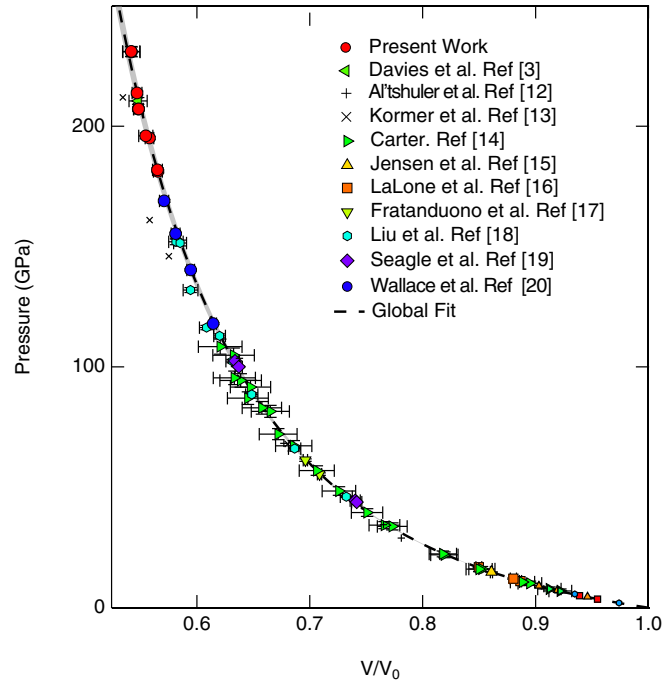

FIG. 9. Stress versus volume compression Hugoniot states for LiF from the current study and from Refs. [3,12–20].

Figure 10(b) shows a graphical representation of the impedance matching for experiment 8. The impact stress (state **1**) corresponds to the intersection of the copper and platinum Hugoniot curves. $P_{\mathrm{Pt}}(u_P)$ is expressed by Eq. (B2)

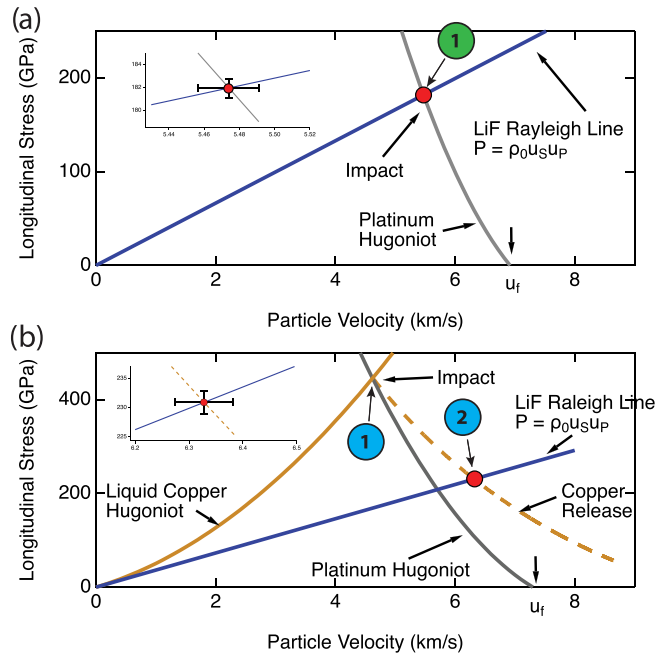

FIG. 10. Graphical representation of impedance matching in the $P - u_P$ plane for (a) Experiment 2 (DI configuration) and (b) Experiment 8 (CuB configuration). (a) State **1** corresponds to the impact state for Pt and LiF. (b) State **1** corresponds to the impact state for Pt and Cu, and state **2** is the state at the Cu/LiF interface.

TABLE IV. Parameters for the linear $U_S(u_P)$ fits used for platinum and copper in the impedance matching calculations.

Material	ρ_0 (g/cm^3)	c_0 (km/s)	S
Pt [43]	21.43 ± 0.03	3.64 ± 0.05	1.54 ± 0.03
Cu [44]	8.930 ± 0.003	4.27 ± 0.08	1.413 ± 0.015

and $P_{\mathrm{Cu}}(u_P)$ is expressed using

$$P_{\mathrm{Cu}}(u_P) = \rho_{0_{\mathrm{Cu}}}(C_{0_{\mathrm{Cu}}} + S_{\mathrm{Cu}}u_P)u_P, \tag{B3}$$

where the coefficients for the copper Hugoniot are given in the Table IV [44]. We note that the impact stresses reached in the copper buffer in experiments 8 and 9 are sufficient to melt the copper [44,45].

The stress in the LiF (state **2**) is determined by the intersection of the LiF Rayleigh line and the copper release curve from state **1** (copper liquid state) discussed next.

3. Copper release isentrope

To determine the release isentrope for liquid copper, we used the Mie-Grüeisen EOS,

$$E - E_H(V) = \frac{1}{\Gamma_V(V)}(P(E,V) - P_H(V)), \tag{B4}$$

where $\Gamma_V(V) = \Gamma(V)/V = (\partial P/\partial E)_V$, and $P_H(V)$ and $E_H(V)$ are the pressure and energy on the Hugoniot respectively. Using an isentrope, $P_S(V) = -(\frac{dE}{dV})_S$, for $P(E,V)$ in Eq. (B4) yields an ordinary differential equation

$$q(V) = \frac{d}{dV}y(V) + p(V)y(V), \tag{B5}$$

where

$$\begin{aligned} y(V) &= P_S(V) - P_H(V) \\ p(V) &= \Gamma_V(V) - \frac{\Gamma_V'(V)}{\Gamma_V(V)} \\ q(V) &= -\Gamma_V(V)\left(P_H(V) + \frac{d}{dV}E_H(V)\right). \end{aligned} \tag{B6}$$

Two approximations are used to simplify Eq. (B5): $\Gamma(V)$ is a linear function of V and the copper Hugoniot data are represented by a linear $U_s - u_p$ relation. These approximations result in:

$$\Gamma(V) = \Gamma_1 V + \Gamma_0, \tag{B7}$$

$$p(V) = \frac{\Gamma_0}{\Gamma_1 V^2 + \Gamma_0 V} + \frac{\Gamma_0}{V} - \Gamma_1, \tag{B8}$$

$$q(V) = \Gamma_V(V)\frac{c_{0_{\mathrm{Cu}}}^2 S_{\mathrm{Cu}}(V_0 - V)^2}{(V_0 - S_{\mathrm{Cu}}(V_0 - V))^3}, \tag{B9}$$

where the linear fit coefficients for copper are given in Table IV.

For experiments 8 and 9, the impact stress in the copper buffer (state **1**) is sufficient to melt it [44,45]. Therefore, we fitted the published Grüneisen parameter for liquid copper [44,45] with a linear equation

$$\Gamma(V) = (33.6 \pm 0.8)\left[\frac{\mathrm{g}}{\mathrm{cm}^3}\right]V - 0.94 \pm 0.05. \tag{B10}$$

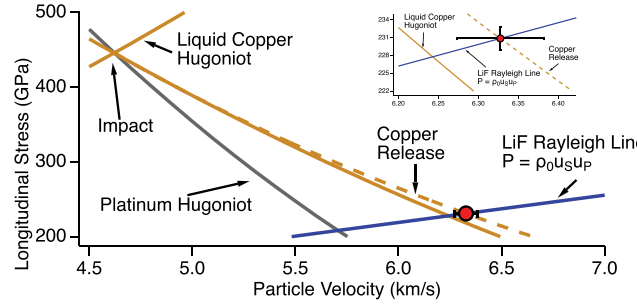

FIG. 11. Impedance matching at the copper/LiF interface using the copper release isentrope (yellow dashed curve). For comparison, the copper reflected Hugoniot curve (yellow solid curve) is also shown.

4. Impedance matching using copper release isentrope

In Fig. 11, we show the LiF peak pressures calculated from two different approaches: use of the release isentrope discussed above and use of the reflected copper Hugoniot. As shown in the Fig. 11 inset, impedance matching using the reflected copper Hugoniot curve (less accurate approach) results in lower stress and lower particle velocity compared to the values (Table II) determined using the copper release isentrope analysis presented above.

[1] M. Furnish, L. Chhabildas, and W. Reinhart, Time-resolved particle velocity measurements at impact velocities of 10 km/s, Int. J. Impact Eng. **23**, 261 (1999).

[2] P. Rigg, M. Knudson, R. Scharff, and R. Hixson, Determining the refractive index of shocked [100] lithium fluoride to the limit of transmissibility, J. Appl. Phys. **116**, 033515 (2014).

[3] J.-P. Davis, M. D. Knudson, L. Shulenburger, and S. D. Crockett, Mechanical and optical response of [100] lithium fluoride to multi-megabar dynamic pressures, J. Appl. Phys. **120**, 165901 (2016).

[4] D. Fratanduono, T. Boehly, M. Barrios, D. Meyerhofer, J. Eggert, R. Smith, D. Hicks, P. Celliers, D. Braun, and G. Collins, Refractive index of lithium fluoride ramp compressed to 800 GPa, J. Appl. Phys. **109**, 123521 (2011).

[5] L. Kirsch, S. Ali, D. Fratanduono, R. Kraus, D. Braun, A. Fernandez-Pañella, R. Smith, J. McNaney, and J. Eggert, Refractive index of lithium fluoride to 900 gigapascal and implications for dynamic equation of state measurements, J. Appl. Phys. **125**, 175901 (2019).

[6] A. B. Belonoshko, R. Ahuja, and B. Johansson, Molecular dynamics of LiF melting, Phys. Rev. B **61**, 11928 (2000).

[7] J. Clérouin, Y. Laudernet, V. Recoules, and S. Mazevet, Ab initio study of the optical properties of shocked LiF, Phys. Rev. B **72**, 155122 (2005).
[8] J. Clérouin, Y. Laudernet, V. Recoules, and S. Mazevet, Ab initio study of optical properties of shock compressed silica and lithium fluoride, J. Phys. A: Math. Gen. **39**, 4387 (2006).
[9] N. Smirnov, Ab initio calculations of the thermodynamic properties of LiF crystal, Phys. Rev. B **83**, 014109 (2011).
[10] X.-W. Sun, Z.-J. Liu, W.-L. Quan, T. Song, R. Khenata, and S. Bin-Omran, High-pressure and high-temperature physical properties of LiF studied by density functional theory calculations and molecular dynamics simulations, J. Phys. Chem. Solids **116**, 209 (2018).
[11] P. C. Myint, E. L. Shi, S. Hamel, H. Cynn, Z. Jenei, M. J. Lipp, W. J. Evans, and M. C. Akin, Two-phase equation of state for lithium fluoride, J. Chem. Phys. **150**, 074506 (2019).
[12] L. Al'tshuler, M. Pavlovskii, L. Kuleshova, and G. Simakov, Investigation of alkali-metal halides at high pressures and temperatures produced by shock compression, Sov. Phys. Solid State **5**, 203 (1963).
[13] S. Kormer, M. Sinitsyn, A. Funtikov, V. Urlin, and A. Blinov, Investigation of the compressibility of five ionic compounds at pressures up to 5 Mbar, Sov. Phys. JETP **20**, 811 (1965).
[14] W. Carter, Hugoniot equation of state of some alkali halides, High Temperatures-High Pressures **5**, 313 (1973).
[15] B. J. Jensen, D. B. Holtkamp, P. A. Rigg, and D. H. Dolan, Accuracy limits and window corrections for photon Doppler velocimetry, J. Appl. Phys. **101**, 013523 (2007).
[16] B. LaLone, O. Fat'yanov, J. Asay, and Y. Gupta, Velocity correction and refractive index changes for [100] lithium fluoride optical windows under shock compression, recompression, and unloading, J. Appl. Phys. **103**, 093505 (2008).
[17] D. Fratanduono, R. Smith, T. Boehly, J. Eggert, D. Braun, and G. Collins, Plasma-accelerated flyer-plates for equation of state studies, Rev. Sci. Instrum. **83**, 073504 (2012).
[18] Q. Liu, X. Zhou, X. Zeng, and S. Luo, Sound velocity, equation of state, temperature and melting of LiF single crystals under shock compression, J. Appl. Phys. **117**, 045901 (2015).
[19] C. T. Seagle, J.-P. Davis, and M. D. Knudson, Mechanical response of lithium fluoride under off-principal dynamic shock-ramp loading, J. Appl. Phys. **120**, 165902 (2016).
[20] M. Wallace, J. Winey, and Y. Gupta, Sound speed measurements in lithium fluoride single crystals shock compressed to 168 GPa along [100], J. Appl. Phys. **130**, 035901 (2021).
[21] J. Liu, L. Dubrovinsky, T. Boffa Ballaran, and W. Crichton, Equation of state and thermal expansivity of LiF and NaF, High Press. Res. **27**, 483 (2007).
[22] H. Dong, S. M. Dorfman, C. M. Holl, Y. Meng, V. B. Prakapenka, D. He, and T. S. Duffy, Compression of lithium fluoride to 92 GPa, High Press. Res. **34**, 39 (2014).
[23] A. Dewaele, Equations of state of simple solids (including Pb, NaCl and LiF) compressed in helium or neon in the Mbar range, Minerals **9**, 684 (2019).
[24] R. Boehler, M. Ross, and D. B. Boercker, Melting of LiF and NaCl to 1 Mbar: Systematics of Ionic Solids at Extreme Conditions, Phys. Rev. Lett. **78**, 4589 (1997).
[25] J. Drabble and R. Strathen, The third-order elastic constants of potassium chloride, sodium chloride and lithium fluoride, Proc. Phys. Soc. **92**, 1090 (1967).
[26] G. Simmons and H. Wang, *Single Crystal Elastic Constants and Calculated Aggregate Properties: A Handbook* (MIT Press, Cambridge, 1971).
[27] S. P. Marsh, *LASL Shock Hugoniot Data* (University of California Press, Los Angeles, 1980).
[28] L. M. Barker and R. E. Hollenbach, Laser interferometer for measuring high velocities of any reflecting surface, J. Appl. Phys. **43**, 4669 (1972).
[29] O. T. Strand, D. R. Goosman, C. Martinez, T. L. Whitworth, and W. W. Kuhlow, Compact system for high-speed velocimetry using heterodyne techniques, Rev. Sci. Instrum. **77**, 083108 (2006).
[30] J. M. Walsh, M. H. Rice, R. G. McQueen, and F. L. Yarger, Shock-wave compressions of twenty-seven metals. Equations of state of metals, Phys. Rev. **108**, 196 (1957).
[31] W. H. Press, S. A. Teukolsky, W. T. Vetterling, and B. P. Flannery, *Numerical Recipes in Fortran 77*, Vol. 1 (Cambridge University Press, Cambridge, 1992).
[32] J. M. Brown and R. G. McQueen, Melting of iron under core conditions, Geophys. Res. Lett. **7**, 533 (1980).
[33] R. S. Hixson, D. A. Boness, J. W. Shaner, and J. A. Moriarty, Acoustic Velocities and Phase Transitions in Molybdenum under Strong Shock Compression, Phys. Rev. Lett. **62**, 637 (1989).
[34] J. H. Nguyen and N. C. Holmes, Melting of iron at the physical conditions of the Earth's core, Nature (London) **427**, 339 (2004).
[35] M. C. Akin, J. H. Nguyen, M. A. Beckwith, R. Chau, W. P. Ambrose, O. V. Fat'yanov, P. D. Asimow, and N. C. Holmes, Tantalum sound velocity under shock compression, J. Appl. Phys. **125**, 145903 (2019).
[36] R. Courant and K. O. Friedrichs, *Supersonic Flow and Shock Waves* (Springer-Verlag, New York, 1976).
[37] Y. B. Zeldovich and Y. P. Raizer, *Physics of Shock Waves and High-Temperature Hydrodynamic Phenomena* (Academic, New York, 1966).
[38] R. G. McQueen, S. P. Marsh, J. W. Taylor, J. N. Fritz, and W. J. Carter, The equation of state of solids from shock wave studies, in *High-Velocity Impact Phenomena* (Academic, New York, 1970), pp. 293–417.
[39] P. Renganathan, T. Duffy, and Y. Gupta, Sound velocities in shock-compressed soda lime glass: Melting and liquid-state response, Phys. Rev. B **104**, 014113 (2021).
[40] M. Wallace, J. Winey, and Y. Gupta, Sound speed measurements in silver shock compressed to 300 GPa: Solid-state transition, melting, and liquid-state response, Phys. Rev. B **104**, 214106 (2021).
[41] P. T. Boggs, R. H. Byrd, and R. B. Schnabel, A stable and efficient algorithm for nonlinear orthogonal distance regression, SIAM J. Sci. Stat. Comput. **8**, 1052 (1987).
[42] J. W. Zwolak, P. T. Boggs, and L. T. Watson, ODRPACK95: A weighted orthogonal distance regression code

with bound constraints, ACM Trans. Math. Softw. **33**, 27 (2007).

[43] N. Holmes, J. Moriarty, G. Gathers, and W. Nellis, The equation of state of platinum to 660 GPa (6.6 Mbar), J. Appl. Phys. **66**, 2962 (1989).

[44] C. A. McCoy, M. D. Knudson, and S. Root, Absolute measurement of the Hugoniot and sound velocity of liquid copper at multimegabar pressures, Phys. Rev. B **96**, 174109 (2017).

[45] D. Hayes, R. Hixson, and R. McQueen, High pressure elastic properties, solid-liquid phase boundary and liquid equation of state from release wave measurements in shock-loaded copper, in *AIP Conference Proceedings*, Vol. 505 (American Institute of Physics, New York, 2000), pp. 483–488.